Introduction

In this study, the time course of *m/z* = 17 at the retention time of methane was monitored for $^{13}CH_4$, which was converted from $^{13}CO_2$. Moreover, the time course of *m/z* = 16 at the same retention time was monitored for $^{12}CH_4$, which was converted from mostly $^{12}CO_2$ by subtracting the $^{13}CH_3^+$ fragment derived from $^{13}CH_4$ (Figure S1).

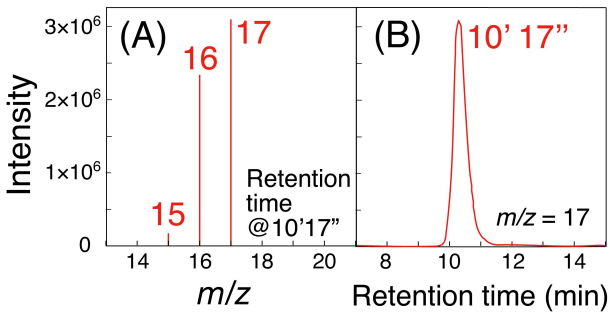

Figure S1. (A) Mass spectrum at 10'17" and (B) mass chromatogram at *m/z* = 17 sampled for 6.0 h under $^{13}CO_2$ (2.3 kPa), H_2 (21.7 kPa), and UV–visible light using the Ni (10 wt%)–ZrO_2-Reduced photocatalyst.

Experimental

ZrO_2 [0.500 g; JRC-ZRO-3, Catalysis Society of Japan; major monoclinic and minor tetragonal phase, specific surface area (SA) 94.4 m^2 g^{-1}] powder and Ni^{II} nitrate hexahydrate (>99.9%, Wako Pure Chemical, Japan; 0.129–0.995 g) were added to water (80 mL, <0.055 μS cm^{-1}) supplied by an RFU424TA system (Advantec, Japan). The mixture was agitated using ultrasound (430 W, 38 kHz) for 20 min and magnetically stirred at 900 rpm for 1 h. Sodium borohydride (>95%, Wako Pure Chemical; 0.129–1.04 g) dissolved in water (20 mL) was added and magnetically stirred at 900 rpm. Then, the suspension was filtered using a polytetrafluoroethene-based membrane filter (Omnipore JVWP04700, Millipore, Burlington, MA, USA; pore size 0.1 μm) and washed with water (250 mL). The resultant powder was dried overnight at 373 K, and is denoted as Ni–ZrO_2. The loading of Ni was between 5.0 and 30 wt%. The 5.0 wt% Ni sample was light green, and the 10–30 wt% Ni samples were grayish-black.

ZrO_2 (0.500 g) and $Ni(NO_3)_2{\cdot}6H_2O$ (0.260 g) were mixed in water, and the water was distilled at 353 K. The resultant powder was dried at 373 K and calcined in air at 723 K for 2 h. The obtained powder is denoted as NiO–ZrO_2, with a Ni loading of 10 wt% and gray color.

For comparison, SiO_2 (mesostructured MCM-41, Sigma–Aldrich, St. Louis, MO, USA; specific SA 1000 m^2 g^{-1}) was used as a support for Ni using a preparation procedure similar to that used for Ni–ZrO_2. The obtained gray powder is denoted as Ni–SiO_2, with a Ni loading of 10 wt%.

The ZrO_2, Ni–ZrO_2, NiO–ZrO_2, or Ni–SiO_2 sample (each 20 mg) was placed in a quartz *U*-tube (internal volume 46.0 mL) connected to a Pyrex glass circulation system (volume 206.1 mL)[1] and treated in vacuum for 1 h using both rotary and diffusion pumps (10^{-6} Pa). Then, 20 kPa of H_2 (purity >99.99%) was introduced into the sample, increased to 723 K at a ramping rate of 15 K min^{-1}, and maintained at the temperature for 10 min. Thus-treated samples are denoted as ZrO_2-Reduced, Ni–ZrO_2-Reduced, NiO–ZrO_2-Reduced, or Ni–SiO_2-Reduced with brownish-black color, although ZrO_2-Reduced was white.

The photocatalytic uptake/exchange/conversion tests of $^{13}CO_2$ were conducted using 20 mg of the catalyst samples. For $^{13}CO_2$ photo-uptake/exchange tests, $^{13}CO_2$ (0.67 kPa; ^{13}C 99.0%, ^{17}O 0.1%, ^{18}O 0.7%, purity >99.9%, Cambridge Isotope Laboratories, Inc., Tewksbury, MA, USA) was used. For $^{13}CO_2$ photoreduction tests, $^{13}CO_2$ (2.3 kPa) and H_2 (21.7 kPa; purity >99.99%) were used. For comparisons, photocatalytic tests under $^{13}CO_2$ (4.6–9.2 kPa) and H_2 (43.4–86.8 kPa) were also performed. Separately, $^{13}CO_2$ (2.3 kPa) and H_2O (2.3 kPa) were introduced for $^{13}CO_2$ photoconversion tests. Furthermore, $^{13}CO_2$ (2.3 kPa), H_2O/D_2O (2.3 kPa, D 99.9%, chemical purity >99.5%, Cambridge Isotope Lab), and H_2 (21.7 kPa) were introduced for $^{13}CO_2$ photoconversion tests.

For these kinetic tests, the quartz reactor containing the catalyst was irradiated with UV–visible light from both top and bottom using a 500 W Xe arc lamp (SX-UID502XAM, Ushio, Japan) through a Y-shaped quartz fiber light guide (Optel, Tokyo, Japan; Model 1.2S15-1000F-1Q7-SP-RX; 40-cm-long fiber and 80-cm-long branches). The distance between the fiber light exit (Φ = 5 mm) and the photocatalyst was 20 mm. The light intensity at the photocatalyst center was 142 mW cm^{-2}. For comparison, $^{13}CO_2$ photoreduction tests were performed under light of 186 mW cm^{-2} in the pressure dependence tests (Table 1c', c", c'''), in the presence/absence of external heat (393 K; Figure 7), and irradiated by full light but in water bath at 295 K (Table 1c"""). The light intensity distribution of the Xe arc lamp on wavelength was measured using a spectroradiometer (Model USR45DA, Ushio, Japan) placed 20 mm from the UV–visible light source (Figure S2).

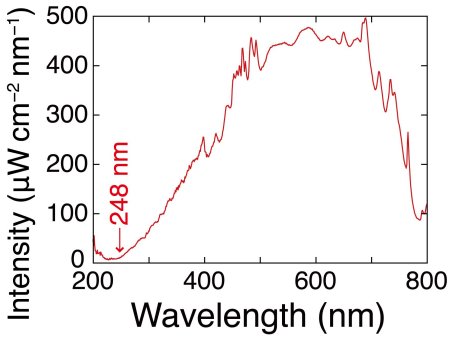

Figure S2. The intensity distribution of light from Xe arc lamp used for kinetic tests in this study as a function of wavelength.

In-profile kinetic data were collected as a function of the light's excitation wavelength by inserting a sharp-cut filter at each fiber light exit. UV32, Y52, and WR715 [2.0, 2.0, and 2.5 mm thick; Hoya, Japan] filters were used to pass light with wavelengths of >320 nm, >520 nm, and >715 nm, respectively. For comparison, a reaction test under dark conditions was conducted by completely wrapping the reactor in Al foil at 298, 373, 393, and 413 K. Furthermore, comparison kinetic test irradiated by full

light but the quartz reactor was in quartz water bath controlled at 295 K was also performed. The kinetic tests irradiated under light at 393 K using $^{13}CO_2$, H_2, (and H_2O) were performed using a quartz fiber light guide and the reactor set in cylindrical heater.

A packed column of polyethene glycol-6000/Flusin P support column (3 m length, 3 mm internal diameter; GL Sciences, Inc., Japan) for $^{13}CO_2$ photouptake/exchange tests and that of 13X-S molecular sieves (3 m length, 3 mm internal diameter; GL Sciences, Inc.) for $^{13}CO_2$ photoreduction/conversion tests were used for online gas chromatography-mass spectrometry (GC-MS) analyses (Model JMS-Q1050GC, JEOL, Tokyo, Japan).[1–3] Helium (0.40 MPa, purity >99.9999%) was used as the carrier gas. A sampling loop (4.6 mL) composed of a Pyrex glass system was maintained under vacuum using rotary and diffusion pumps (10^{-6} Pa) and connected to GC-MS through deactivated fused silica tubes (No. 160-2845-10, Agilent, Santa Clara, CA, USA; 1.5 m, internal diameter 250 μm), which were maintained at 393 K during the analysis to avoid gas adsorption.

The surface species were monitored with a single-beam Fourier transform infrared (FTIR) instrument (JASCO, Tokyo, Japan; Model FT/IR-4200) equipped with a mercury–cadmium–tellurium-M detector at a constant temperature of 77.4 K.[1,4,5] A self-supporting disk (Φ = 20 mm) of Ni (10 wt%)–ZrO_2-Reduced (10 mg) diluted with ZrO_2 (90 mg) was prepared in a Pyrex tube and transferred into a quartz photoreaction IR cell equipped with NaCl windows on both sides using a glove box (model MINI 400RS; Unico, Tsukuba, Japan) filled with argon (purity >99.998%). The cell was connected to the Pyrex glass circulation system, as well as to the GC-MS, to enable simultaneous monitoring of the surface species using FTIR and isotope distribution in products using GC-MS.[1,2] The photocatalyst disk was evacuated (10^{-6} Pa) at 295 K for 2 h prior to the measurements.

The in-situ FTIR measurements were performed at 295 K in a range of 4000–650 cm^{-1}. The sample disk was irradiated with UV–visible light by a 500 W Xe arc lamp using a quartz fiber light guide. The distance between the fiber light exit and sample disk was 46 mm. The light intensity at the sample center was 90 mW cm^{-2}. The spectrometer's energy resolution was 1 cm^{-1}, and the data accumulation included 256 scans (~2 s per scan). From each spectrum, we subtracted the spectrum of Ni (10 wt%)–ZrO_2 just reduced in H_2 at 723 K.

UV−visible spectra were recorded on a double-beam model V-650 spectrophotometer using D_2 and halogen lamps below and above 340 nm, equipped with a photomultiplier tube and an integrated ISV-469 sphere (JASCO, Tokyo, Japan) for diffuse-reflectance detection within the wavelength range of 200–800 nm.[1,2] The data were transformed using the Kubelka–Munk function. A polytetrafluoroethene plate was used as the reference.

Transmission electron microscopy (TEM) was performed using a JEM-2100F (JEOL) equipped with a field-emission gun (acceleration voltage of 200 kV) at the Center for Analytical Instrumentation. The samples were mounted on a Cu mesh (250 meshes per inch) coated with carbon and a copolymer film of poly(vinyl alcohol) and formaldehyde (Formvar, Monsanto, St. Louis, MO, USA). High-angle annular dark-field (HAADF) scanning TEM (STEM) and high-resolution (HR) TEM images were observed using the JEM-2100F model.[1] The chemical compositions and elemental distributions were analyzed using energy-dispersive spectra with a Si (Li) detector equipped in the TEM.[4]

X-ray diffraction (XRD) patterns were observed using a D8 ADVANCE diffractometer (Bruker, Billerica, MA, USA) at the Center for Analytical Instrumentation at a Bragg angle (θ_B) of $2\theta_B$ = 20°–60° with a scan step of 0.02° and scan rate of 1 s per step. The measurements were performed at 40 kV and 40 mA using Cu Kα emission (wavelength λ = 0.15419 nm) and a Ni filter. The crystal sizes (t) were estimated using the following Scherrer equation:

$$t = \frac{0.9\lambda}{\text{Peak width} \times \cos\theta_B} \quad \text{(S1)}$$

The absorption–fluorescence spectra were recorded on FP-8600 (JASCO; Chiba Iodine Resource Innovation Center) using a 150 W Xe arc lamp (UXL-159, Ushio) equipped with a photomultiplier tube for excitation at 200–300 nm within a fluorescence range of 300–800 nm. The incident excitation light from Xe lamp was monitored by Si photodiode, and monitored fluorescence light emitted from sample was normalized based on the incident light intensity at each wavelength. The photocatalyst powder (2.0 mg) was mixed with purified water (3.0 mL) and ultrasonicated (430 W, 38 kHz) for 30 min. All spectra were recorded for the suspensions in a quartz cell at 295 K.

The Ni K-edge extended X-ray absorption fine structure (EXAFS) spectra were measured at 295 K in the transmission mode at the Photon Factory, High Energy Accelerator Research Organization (KEK, Tsukuba, Japan), on 9C and 12C beamlines. A Si(1 1 1) double-crystal monochromator and a Rh-coated focusing bent cylindrical mirror were inserted into the X-ray beam path. A piezotransducer was used to detune the X-ray to two-thirds of the maximum intensity to suppress the higher harmonics. The Ni K-edge absorption energy was calibrated at 8331.65 eV[6] using the spectrum of Ni metal (5.0 μm thick).

The Ni, Ag, and Mo K-edge EXAFS spectra were measured for Ni, Ag, and Mo foils at 300–400 K on 9C beamline and at the Photon Factory Advanced Ring, KEK, on NW10A beamline equipped with a Si(3 1 1) double-crystal monochromator, a Pt-coated focusing bent cylindrical mirror, and a piezotransducer.[1]

Ni (10 wt%)–ZrO_2-Reduced powder (120 mg) was prepared in a Pyrex glass *U*-tube, and transferred into a Pyrex glass XAFS cell (Φ = 20 mm, t = 2.0 mm) equipped with polyethene terephthalate (PET) film windows (Toyobo Film Solutions, Japan, G2; 38 μm thick) for both UV–visible light and X-ray transmission. The cell was directly connected to the *U*-tube, and the sample did not contact air throughout the procedure. Then, the XAFS cell was filled with the reactant gas. The sample was then irradiated with UV–visible light from the Xe arc lamp through a quartz fiber light guide and the PET film window at the beamline. X-rays were perpendicularly transmitted from the disk, whereas the incident angles of UV–visible light were 45° and −135° relative to the X-rays.[1–3,7] The distance between the light exit of the quartz fiber light guide and the sample was 50 mm.

The obtained Ni K-edge EXAFS data were analyzed using XDAP,[8] and the pre-edge background was approximated with a modified Victoreen function:

$$\frac{C_2}{E^2} + \frac{C_1}{E} + C_0 \quad \text{(S2)}$$

where E is the photon energy. The background for post-edge oscillation, μx, was approximated with a smoothing spline function and calculated for a particular number of datapoints:

$$\sum_{i=1}^{\text{Data Points}} \frac{(\mu x_i - \text{background}_i)^2}{\exp\left(-0.075k_i^2\right)} \leq \text{smoothing factor} \quad \text{(S3)}$$

in which k is the angular photoelectron wavenumber.

Multiple-shell curve-fit analyses were performed on the Fourier-filtered k^3-weighted EXAFS data in k– and R-space (R is interatomic distance) based on the plane-wave approximation (eq. 7 in main text) using an XDAP code,[8] in which the empirical amplitude was extracted from the EXAFS data for the Ni metal foil and NiO powder. The R values for the Ni–Ni interatomic pair were set to 0.24917 nm with an N value of 12 for Ni metal (a = 0.35238 nm),[9] and those for the Ni–O and Ni–Ni interatomic pair were set to 0.2088 nm with an N value of 6 and to 0.2953 nm with an N value of 12 for NiO (a = 0.4176 nm).[10] We assumed that the many-body reduction factor, S_0^2, was identical for both sample and reference.

Results and Discussion

1. $^{13}CO_2$-EXCHANGE REACTION AND PHOTOREDUCTION

ZrO_2 not pretreated with H_2 only formed CO (Table S1a); however, the CO formation rate increased by 1.16 times after H_2 treatment (Figure 1A and Table 1a).

Moreover, the Ni (10 wt%)–ZrO_2 photocatalyst was tested for CO_2 photoreduction (Table S1b). The total formation rate of C-containing compounds, mostly methane, was only 0.97% of that using Ni (10 wt%)–ZrO_2-Reduced (Figure 1C). However, the initial rate increased by 3.1 times at 42–47 h. This is because the oxidized Ni^{II} sites of Ni (10 wt%)–ZrO_2 gradually transformed into Ni^0 under H_2 and UV–visible light.

Based on the uptake/exchange tests conducted for $^{13}CO_2$ (0.67 kPa; Figure 2A), the equilibrated $^{12}CO_2$ ratio was 2.4 mol% in total CO_2 gas, using 20 mg of ZrO_2-Reduced. Therefore, the equilibrated $^{13}CO_2$ and $^{12}CO_2$ on the surface were 9.8 μmol (Figure 2A) and $9.8 \times 0.024 = 0.23$ μmol for ZrO_2-Reduced. Thus, the amount of $^{12}CO_2$ that existed on the surface before the photo-uptake/exchange test conducted on ZrO_2-Reduced (20 mg) was 0.23 − 0.098 + 0.66 = 0.79 μmol (Figure 2A). The equilibrated $^{12}CO_2$ ratio during the photocatalytic reduction tests conducted using 2.3 kPa of $^{13}CO_2$ (193 μmol, ^{13}C 99.0%) and ZrO_2-Reduced (20 mg) was $(1.93 + 0.79)/193 = 1.4$ mol%.

Similarly, based on Figure 2B, the equilibrated $^{12}CO_2$ ratio was 2.1 mol% in total CO_2 gas using 0.67 kPa of $^{13}CO_2$ and 20 mg of Ni (10 wt%)–ZrO_2-Reduced. The equilibrated $^{13}CO_2$ and $^{12}CO_2$ on the surface were 5.9 μmol (Figure 2B) and $5.9 \times 0.021 = 0.12$ μmol, respectively, over Ni (10 wt%)–ZrO_2-Reduced. Thus, the amount of $^{12}CO_2$ on the surface before the photouptake/exchange test conducted on Ni (10 wt%)–ZrO_2-Reduced (20 mg) was 0.12 – 0.02 + 0.54 = 0.64 μmol (Figure 2B). The equilibrated $^{12}CO_2$ ratio during the photocatalytic reduction tests conducted using 2.3 kPa of $^{13}CO_2$ (193 μmol, ^{13}C 99.0%) and Ni (10 wt%)–ZrO_2-Reduced (20 mg) was $(1.93 + 0.64)/193 = 1.3$ mol%.

In contrast, based on ref. 1, the equilibrated $^{12}CO_2$ ratio was 7.3 mol% for the total CO_2 gas using 0.67 kPa of $^{13}CO_2$ and 100 mg of ZrO_2, not H_2-reduced. The equilibrated $^{13}CO_2$ and $^{12}CO_2$ on the surface were 19.8 μmol (Figure 2B) and $19.8 \times 0.073 = 1.4$ μmol over ZrO_2. Thus, the amount of $^{12}CO_2$ on surface before the photouptake/exchange test conducted on ZrO_2 (100 mg) was 1.4 + 2.3 = 3.7 μmol. This corresponds to 0.74 μmol per 20 mg ZrO_2, essentially equivalent to 0.79 μmol for ZrO_2-Reduced. Thus, the H_2-pretreatment of ZrO_2 at 723 K affected exclusively the amount of chemisorbed CO_2 over ZrO_2-Reduced (0.66 μmol; Figure 2A) versus ZrO_2 (0.45 μmol per 20 mg ZrO_2).[1] This difference is the difference of O vacancy sites over ZrO_2 (Scheme 1A-c), and accounts for the increase of CO formation rate by 1.16 times (Tables 1a and S1a).

In the $^{13}CO_2$ photoreduction tests, the ^{13}C ratio in the formed C-containing products was 2.1–4.3 mol% when no filter or a filter to transmit λ > 320 nm was used (Table 1c, c""), and gradually increased to 5.7, 29, and 34 mol% when a filter to transmit λ > 520 and 715 nm was used and under dark conditions, respectively (Table 1c'''', c""", c'''''''). The exchange of free $^{13}CO_2$ with $^{12}CO_2$ chemisorbed from air became substantially slower under light of longer wavelength, and under dark conditions, and the contribution of $^{12}CO_2$ originating from the air (Scheme 1A-c) became not negligible.

Using NiO (10 wt% Ni)–ZrO_2-Reduced, the formation rate of the total C-containing compounds increased by a factor of 1200 after H_2 pretreatment (Table S1c and Figure S5B), which was 66% of that using Ni (10 wt%)–ZrO_2-Reduced (Table 1c). The difference could be owing to the difference in particle size of Ni^0 formed either by $NaBH_4$ or by heating in H_2 at 723 K.

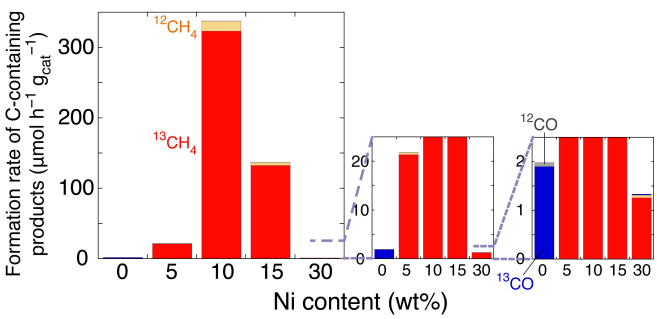

Figure S3. Formation rate dependences of $^{13}CH_4$, $^{12}CH_4$, ^{13}CO, and ^{12}CO on the Ni content in ZrO_2 in the photocatalytic test exposed to $^{13}CO_2$ (2.3 kPa) and H_2 (21.7 kPa). The catalysts were previously reduced in H_2 at 723 K.

Table S1. Kinetic data on photoconversion of $^{13}CO_2$ (2.3 kPa) using H_2 (21.7 kPa) and the ZrO_2-based photocatalysts (0.020 g) under UV–visible light

Entry	Catalyst	Formation rate (μmol-C h^{-1} g_{cat}^{-1})					^{12}C-product ratio (mol%)
		^{13}CO	^{12}CO	$^{13}CH_4$	$^{12}CH_4$	Σ C-containing compounds	
a	ZrO_2	1.1	0.64	<0.002	<0.002	1.7	37
b	Ni (10 wt%)–ZrO_2	0.11	<0.002	2.6	0.60	3.3	18
c	NiO (10 wt% Ni)–ZrO_2-Reduced	0.020	<0.002	220	1.6	220	0.73

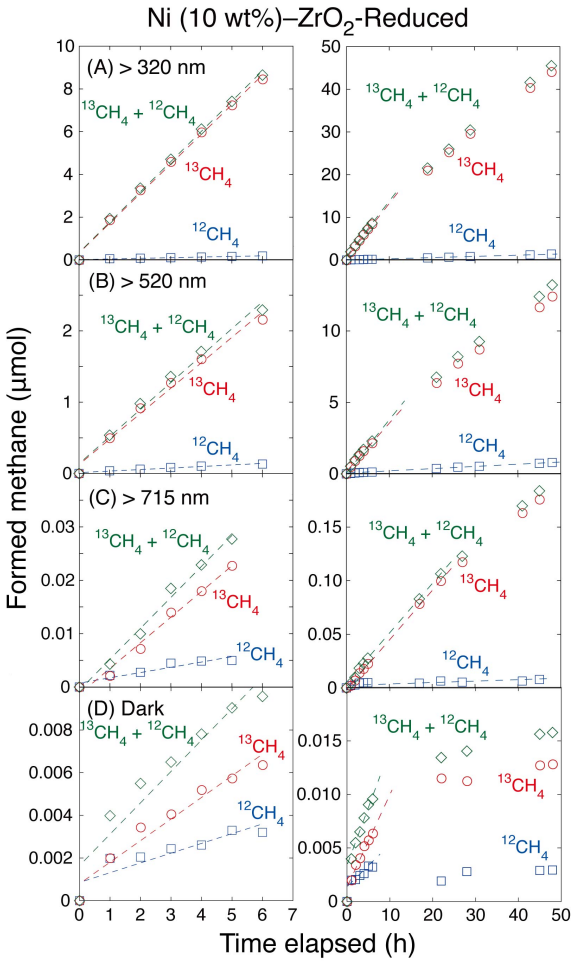

Figure S4. Time course of $^{13}CH_4$ and $^{12}CH_4$ formation during (A–C) photocatalytic and (D) catalytic tests exposed to $^{13}CO_2$ (2.3 kPa) and H_2 (21.7 kPa) using Ni (10 wt%)–ZrO_2-Reduced. (A–C) Catalyst was irradiated under Xe arc lamp filtered at wavelengths (A) λ > 320 nm, (B) λ > 520 nm, and (C) λ > 715 nm and (D) catalyst under dark conditions at 298 K. The amount of catalyst used was 0.020 g.

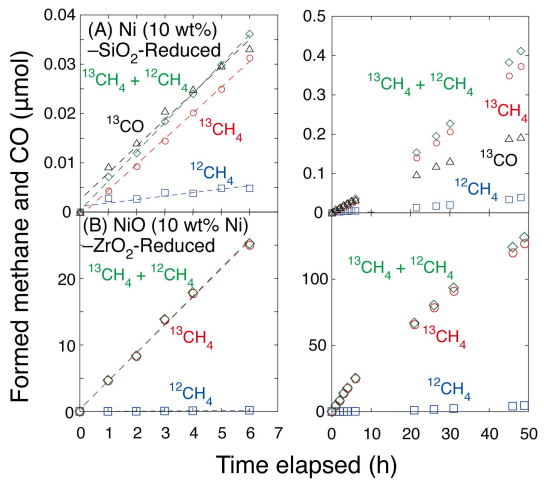

Figure S5. Time course of ^{13}CO, ^{12}CO, $^{13}CH_4$, and $^{12}CH_4$ formation during the photocatalytic test exposed to $^{13}CO_2$ (2.3 kPa) and H_2 (21.7 kPa) using (A) Ni (10 wt%)–SiO_2-Reduced and (B) NiO (10 wt% Ni)–ZrO_2-Reduced. The amount of catalyst used was 0.020 g.

2. UV–VISIBLE ABSORPTION SPECTRA

The UV–visible spectrum for ZrO_2 contained edge absorption at 248 nm (Figure S6). The spectrum for Ni (5.0 wt%)–ZrO_2 was similar to that for ZrO_2. However, a weak shoulder (250–290 nm) to the absorption edge and a tiny peak centered at 404 nm appeared. The spectrum suggested that the Ni nanoparticles formed through a liquid-phase reduction, partially re-oxidized.

The Ni (5.0 wt%)–ZrO_2-Reduced sample showed extensive absorption in the entire wavenumber region of 200–800 nm (Figure S6), suggesting the presence of Ni^0.

Unlike Ni (5.0 wt%)–ZrO_2, Ni (10 wt%)–ZrO_2 exhibited substantial absorption over the whole wavelength region in Figure S6. The difference suggested that the Ni^0 nanoparticles formed through a liquid-phase reduction were relatively stable in air probably owing to the difference in pH during the liquid-phase reduction and the resultant particle size of Ni.

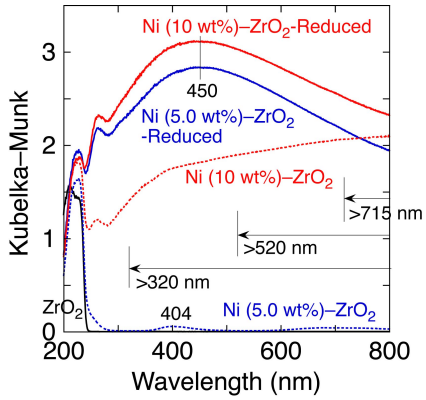

Figure S6. Diffuse-reflectance UV–visible absorption spectra for ZrO_2, Ni (5.0 wt%)–ZrO_2, Ni (5.0 wt%)–ZrO_2-Reduced, Ni (10 wt%)–ZrO_2, and Ni (10 wt%)–ZrO_2-Reduced samples.

3. FTIR MONITORING UNDER $^{13}CO_2$ AND H_2

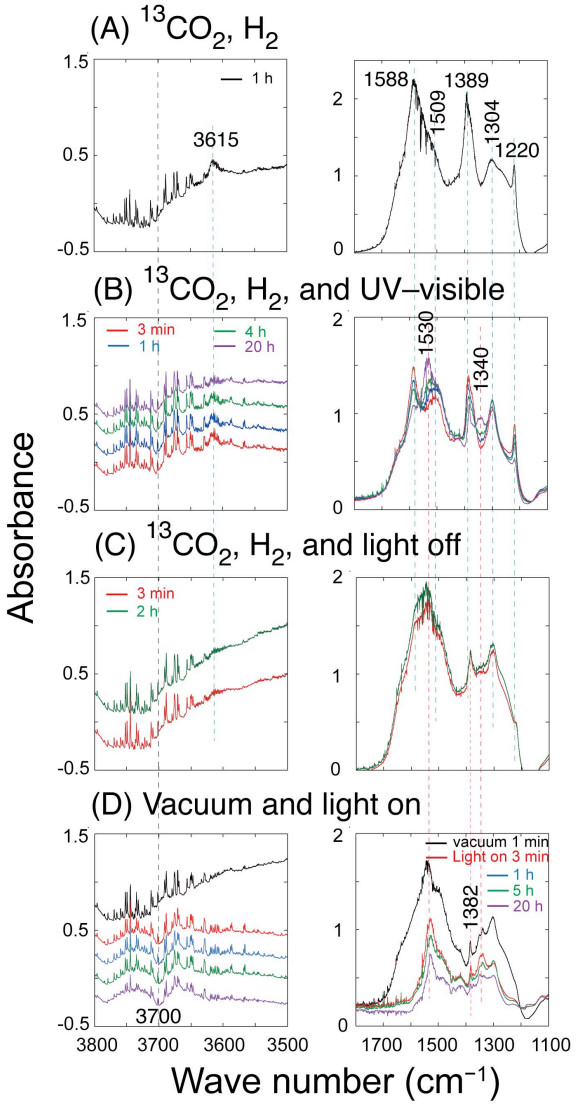

Figure S7. FTIR spectra of Ni (10 wt%)–ZrO_2-Reduced (10 mg) in wavenumber regions of 3800–3500 cm^{-1} (left) and 1800–1100 cm^{-1} (right). (A) Under $^{13}CO_2$ (2.3 kPa) and H_2 (21.7 kPa) for 1 h. (B) Under $^{13}CO_2$, H_2, and UV–visible light for 20 h. (C) Under $^{13}CO_2$, H_2, and darkness for 2 h. (D) Under vacuum for 1 min, and then UV–visible light for 20 h. The spectrum for Ni (10 wt%)–ZrO_2 just reduced in H_2 at 723 K was subtracted from each data.

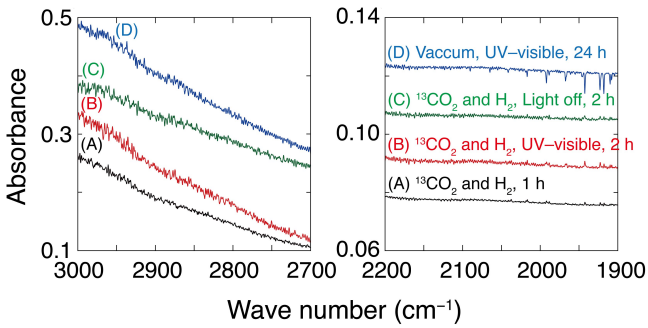

Figure S8. FTIR spectra of ZrO_2 (50 mg) for 3000–2700 cm^{-1} (left) and 2200–1900 cm^{-1} (right). The spectrum for fresh ZrO_2 was subtracted from each data. (A) Under $^{13}CO_2$ (2.3 kPa) and H_2 (21.7 kPa) for 1 h. (B) Under $^{13}CO_2$, H_2, and UV–visible light for 2 h. (C) Under $^{13}CO_2$, H_2, and darkness for 2 h. (D) Under vacuum for 1 min, and then UV–visible light for 24 h.

4. TEM OBSERVATION

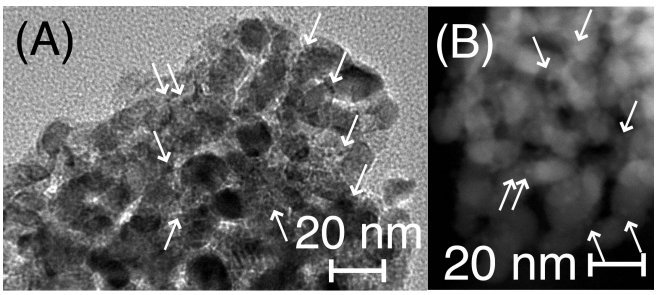

Figure S9. (A) TEM and (B) HAADF-STEM images observed for Ni (10 wt%)–ZrO_2-Reduced sample. The arrows indicate Ni nanocrystals dispersed on ZrO_2 crystals.

5. XRD

In the XRD pattern for the incipient Ni–ZrO_2-Reduced samples (Figure S10), the diffraction peaks at 24.3°, 28.1°, 31.4°, 34.3°, 35.3°, 38.7°, 41.0°, 45.1°, 50.3°, 54.2°, and 55.7°, assignable to (1 1 0), ($\bar{1}$ $\bar{1}$ 1), (1 1 1), (0 2 0), (2 0 0), (1 2 0), (1 0 2), ($\bar{2}$ 0 2), ($\bar{1}$ 2 2), (3 0 0), and (1 3 0) planes of monoclinic crystal of ZrO_2, respectively, were observed. When the Ni content was >10 wt%, two new peaks appeared at 44.4° and 51.8°, assigned to (1 1 1) and (2 0 0) planes of Ni metal, respectively (Figure S10).

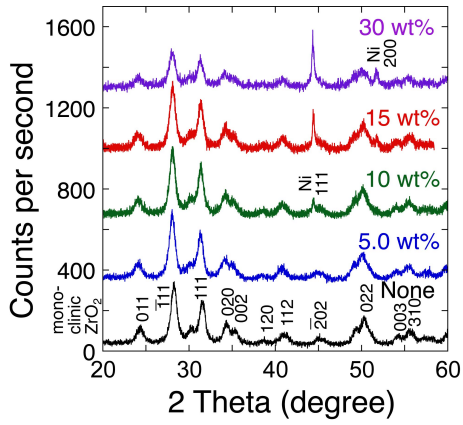

Figure S10. XRD patterns of Ni–ZrO_2-Reduced. The Ni content was 0, 5.0, 10, 15, and 30 wt%.

6. FLUORESCENCE SPECTRA

Ni–ZrO_2-Reduced samples were all brownish-black, where Ni^0 absorbed most part of UV–visible light while ZrO_2 mostly absorbed UV light of λ < 248 nm (Figures S2 and S6). The intensity at 370 nm decreased by 72% and 90% with the addition of 5.0 and 30 wt% of Ni, respectively (Figure 5A), as the Ni species shielded ZrO_2 from the incident light and also

accepted and isolated the photoelectrons from ZrO_2 (charge transfer), to suppress the competing fluorescence emission step.

Figure 5B shows the weaker fluorescence above 248 nm caused by the low concentration of O vacancy level between the ZrO_2 bandgaps. The fluorescence with the excitation at 248 nm was clearly confirmed for ZrO_2 (Figure S11B), while it was quite suppressed due to the charge separation with Ni nanocrystals for Ni (10 wt%)–ZrO_2-Reduced (Figure S11B). Using Xe arc lamp and quartz cell both for kinetic tests (Figure 1) and fluorescence spectroscopy (Figures 5 and S11), ZrO_2 could be excited via band-gap excitation near the foot of wavelength distribution for Xe lamp (λ < 248 nm; Figure S2) and also the electronic transition related to the O vacancy of ZrO_2 (λ > 248 nm; Figures 5B and S11B).

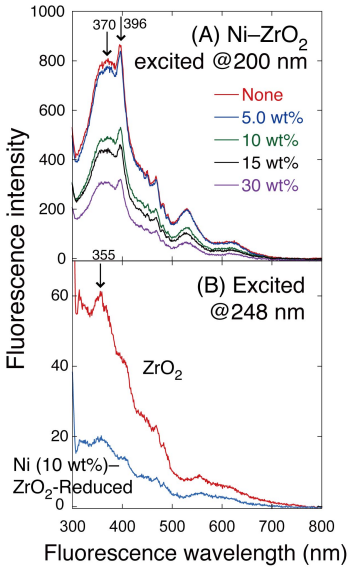

Figure S11. Fluorescence spectra for (A) Ni (0–30 wt%)–ZrO_2 with the excitation at 200 nm and (B) ZrO_2 and Ni (10 wt%)–ZrO_2-Reduced with the excitation at 248 nm; 2 mg of the sample powder was suspended in 3 mL of water.

7. Ni K-EDGE EXAFS

The intensity of the Ni–Ni shell at 0.21 nm (phase shift uncorrected) for Ni (5.0 wt%)–ZrO_2-Reduced was similar to that for Ni metal, and decreased by 44% when exposed to air for 1 week, suggesting that Ni^0 core remained inside the $Ni^{II}O$ shell.

Moreover, the change in the Ni K-edge EXAFS for Ni (5.0 wt%)–ZrO_2-Reduced photocatalyst irradiated by UV–visible light was monitored (Figure S12) in comparison to that for Ni (10 wt%)–ZrO_2-Reduced photocatalyst (Figure 6). The $\sigma_{disorder}$ value was evaluated as 0.00292 nm. Then, the temperature at the Ni site based on the σ values was evaluated. Based on the mean N(Ni–Ni) value (7.1) for Ni (5.0 wt%)–ZrO_2-Reduced, the mean particle size of 1.1 nm and dispersion of 0.77 were evaluated. The temperature rise (372–388 K) using Ni (5.0 wt%)–ZrO_2-Reduced decreased by >10 K compared to 389–394 K using Ni (10 wt%)–ZrO_2-Reduced (Table S2a, b).

The reason why methane formation drew a curve peaked at Ni 10 wt% in photocatalytic tests exposed to $^{13}CO_2$ and H_2 (Figure S3) is considered. The rate using Ni (10 wt%)–ZrO_2-Reduced was higher by a factor of 16 times compared to one using Ni (5.0 wt%)–ZrO_2-Reduced (Table 1b, c) because of (i) the increase of active Ni sites, (ii) Ni^0 site temperature difference by >10 K, (iii) relatively stable Ni^0 state @10 wt% in contrast to the oxidized Ni^{II} sites in air @5.0 wt% (Figure S6), and (iv) the quantum size effects of the Ni particles (mean 1.7 nm@10 wt% versus 1.1 nm @5.0 wt%). Conversely, when the Ni amount became more than 10 wt%, the Ni nanocrystals predominantly covered ZrO_2 surface (Figures 5A and S11). By the effects, the first step from CO_2 to CO over ZrO_2 surface was significantly suppressed and methane formation rate drastically dropped (Figure S3).

The temperature dependence of experimental σ values for metal foils as examples agreed well with that by theory.[11] We confirmed the deviation between experiment and theory was <8 K for metal foils in the range of 300–400 K (Figure S13), and applied to the local temperature evaluation of mean 1.7 nm Ni nanocrystals based on correlated Debye model.[11,12] Taking systematic error to experimentally determine σ value led to the error <20 K (Figure 6D) into account, total evaluation errors as root mean square would be <22 K (Scheme 1C). Anyway, to monitor the local temperature of 1.1 or 1.7 nm Ni nanocrystals dispersed on ZrO_2 by thermocouple is impossible.

When the Ni (10 wt%)–ZrO_2-Reduced was irradiated under light of λ > 320 nm (Figure S14, left), the trend of changes in N and σ values was similar to that of the data irradiated under full light (Figure 6C, D). The temperature increased to 378–387 K (Figure S14D, left). The mean temperature was lower by <10 K than that irradiated by full light (Table S2b, c). In contrast, the temperature reached during irradiation of light of λ > 715 nm was 322–334 K (Figure S14D, right, and Table S2d).

Figure S15 shows the monitoring of Ni sites in the Ni (10 wt%)–ZrO_2-Reduced photocatalysts under CO_2 and moisture where a reversible temperature change is observed. Table S2e lists the conditions and temperature obtained.

The increase in temperature for the Ni, Ag, and Au sites, combined with ZrO_2 irradiated by light, is summarized in Table S2. The reversible temperature rise was primarily controlled by the incident light wavelengths for Ni (b–d), Ag (h–j), and Au (k, l). The increase in Ni and Ag ratio in the composites slightly increased the temperature. The temperature rise was in the order Ni > Ag > Au (Table S2b, f, k), and did not correlate to the molar heat capacity C_p^e value of metals. Brownish–black Ni nanoparticles of 1–2 nm absorbed visible light more effectively than the localized surface plasmon resonance[13] of Ag and Au nanoparticles (mean 3–4 nm), and enabled Ni to have a temperature of 394 K (Figure 6D).

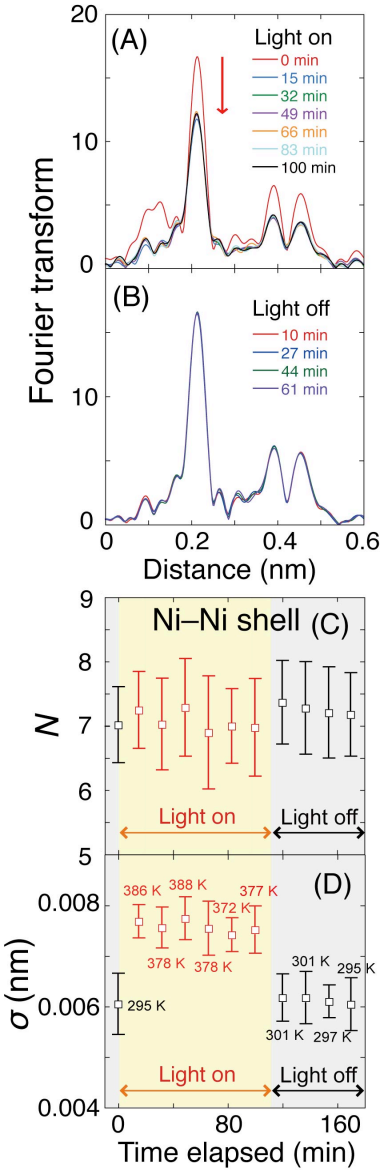

Figure S12. Ni K-edge EXAFS for Ni (5.0 wt%)–ZrO_2-Reduced under CO_2 (2.3 kPa) and H_2 (21.7 kPa). (A, B) Time-course change of Fourier transform of $k^3\chi$ irradiated by light from Xe arc lamp (A) and under dark conditions (B). (C, D) N (C) and σ values (D) obtained by curve-fit analyses for the Ni–Ni shell at 0.21 nm in panels A and B.

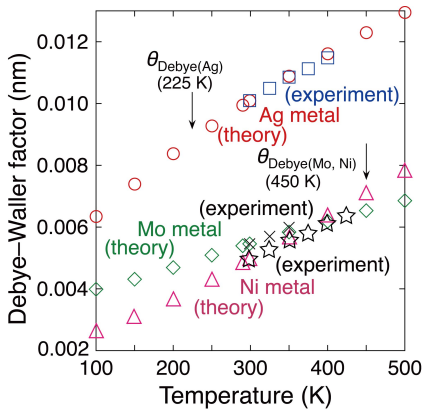

Figure S13. The temperature dependence of Debye–Waller factor for Ag, Mo, and Ni metal foils (a) monitored by thermocouple in an electric furnace at constant temperature (square, □; cross, ×; star, ☆) and (b) generated by the correlated Debye model using a FEFF8.4 code (circle, ○; diamond, ◇; triangle, △).

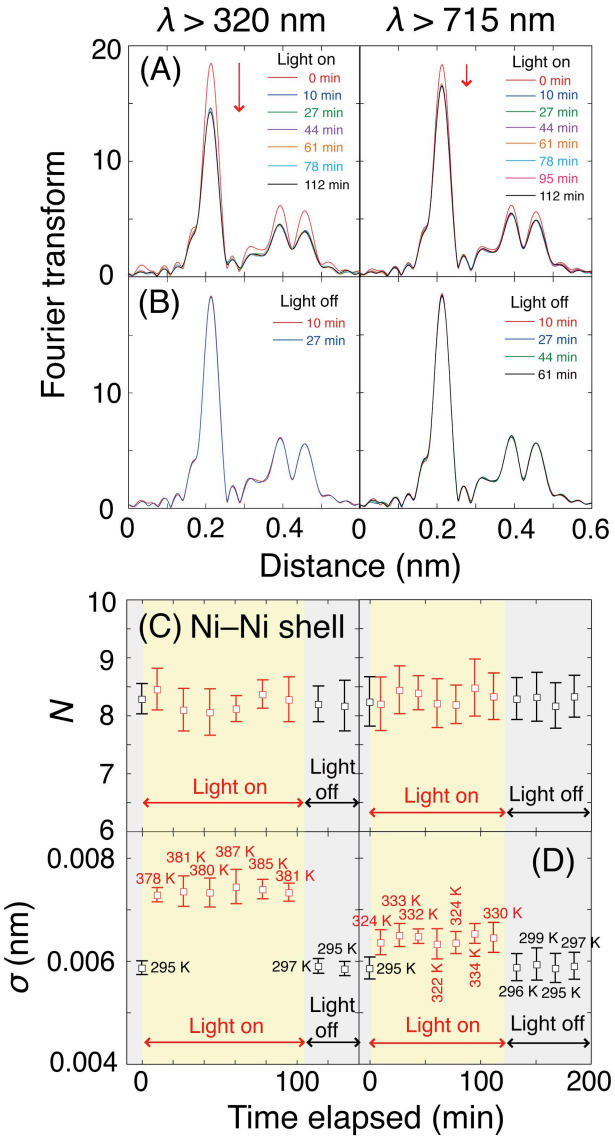

Figure S14. Ni K-edge EXAFS for Ni (10 wt%)–ZrO_2-Reduced under CO_2 (2.3 kPa) and H_2 (21.7 kPa). (A, B) Time-course change of Fourier transform of $k^3\chi$ irradiated by light from Xe arc lamp filtered at λ > 320 nm (Left panel) and λ > 715 nm (Right panel) (A) and under dark (B). (C, D) N (C) and σ values (D) obtained by curve-fit analyses for the Ni–Ni shell at 0.21 nm in panels A and B.

Table S2. Temperature of metal (Ni, Ag, and Au)–ZrO_2 photocatalyst samples monitored by EXAFS and related factors

Entry	Metal				Sample amount (mg)	Sample color	Purged gas	Light irradiated	T_{heated} (K)	Ref
	Element	Content (wt%)	$C_p^{\ominus}$ (J K^{-1} g^{-1})	θ_{Debye} (K)						
a	Ni	5.0	0.444	450	120	Brownish black	CO_2 (2.3 kPa), H_2 (21.7 kPa)	Full light	372–388	This work
b		10						Full light	389–394	
c								λ > 320 nm	378–387	
d								λ > 715 nm	322–334	
e							CO_2 (2.3 kPa), H_2O (2.3 kPa)	Full light	378–384	
f	Ag	3.0	0.235	225	125	Dark yellow	CO_2 (2.3 kPa), H_2 (21.7 kPa)		325–392	1
g							Argon		348–367	
h		5.0					CO_2 (2.3 kPa), H_2 (21.7 kPa)		351–363	
i								λ > 320 nm	331–365	
j								λ > 580 nm	307–329	
k	Au	5.0	0.129	165	80	Wine red		Full light	314–321	2
l								λ > 715 nm	299–300	
m							Argon	Full light	320–324	

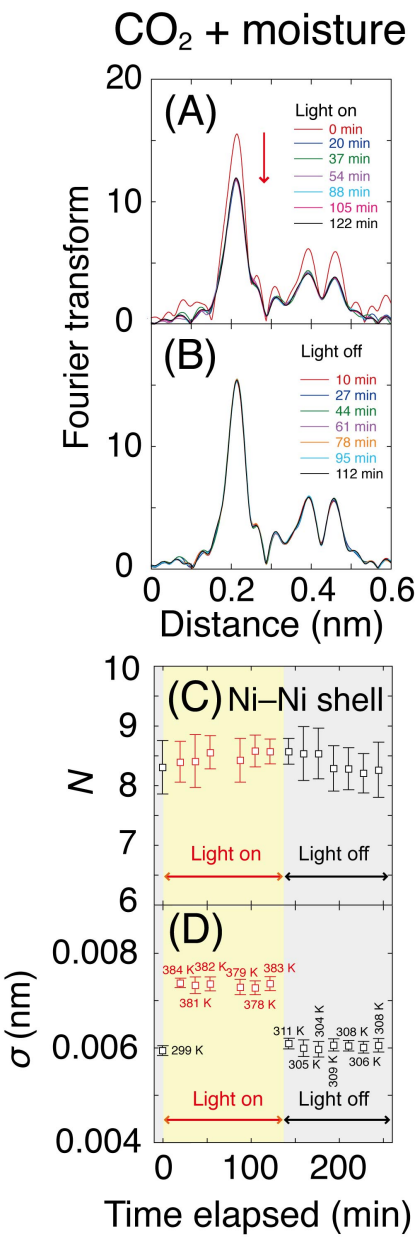

Figure S15. Ni K-edge EXAFS for Ni (10 wt%)–ZrO_2-Reduced under CO_2 (2.3 kPa) and H_2O (2.3 kPa). (A, B) Time-course change in Fourier transform of $k^3\chi$ irradiated by light from Xe arc lamp (A) and under dark (B). (C, D) Coordination number N (C) and Debye–Waller factor σ (D) obtained by curve-fit analyses for the Ni–Ni shell at 0.21 nm in panels A and B.

8. $^{13}CO_2$ PHOTOCONVERSION IN H_2 AND H_2O/D_2O

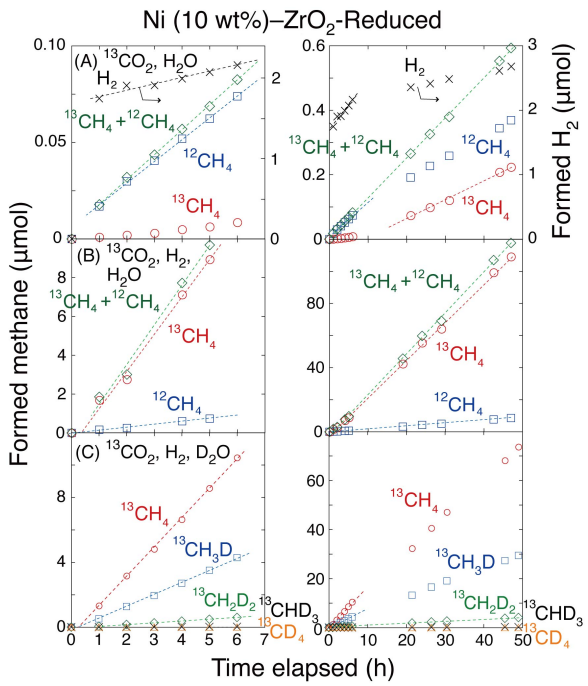

Figure S16. Time course of $^{13}CH_4$, $^{12}CH_4$, and H_2 formation during the photocatalytic test with (A) $^{13}CO_2$ (2.3 kPa) and H_2O (2.3 kPa), (B) $^{13}CO_2$ (2.3 kPa), H_2 (21.7 kPa), and H_2O (2.3 kPa), and (C) $^{13}CO_2$ (2.3 kPa), H_2 (21.7 kPa), and D_2O (2.3 kPa) using Ni (10 wt%)–ZrO_2-Reduced (0.020 g).

Finally, we tested CO_2 photoconversion using water and Ni (10 wt%)–ZrO_2-Reduced catalyst (eq. 3 of main text). H_2 was quickly formed in the initial 1 h by the stoichiometric oxidation of Ni^0 surface by H_2O (Figure S16A, left), but the subsequent, steady photocatalytic reduction rate of water was 3.8 μmol h^{-1} g_{cat}^{-1} (Table 2a). In contrast, CH_4 was formed constantly from the beginning, but the preferable $^{12}CH_4$ formation switched to both $^{13}CH_4$ and $^{12}CH_4$ formation at ~10 h of the reaction. The total formation rate of the C-containing products, mostly methane, was only 0.23% of that obtained using H_2 (Tables 1c and 2a).

Based on Table S3, the following correlations were obtained for the kinetic tests in $^{13}CO_2$, H_2, and D_2O.

$$e = E$$

$$d \simeq D$$

$$c \simeq C - \left(\frac{1}{4}D + E\right)f$$

$$b \simeq B - \left(\frac{1}{2}C + \frac{3}{4}D\right)f + \left(\frac{1}{8}D + \frac{1}{2}E\right)f^2$$

$$a \simeq A - \left(\frac{3}{4}B + \frac{1}{2}C\right)f + \left(\frac{3}{8}C + \frac{11}{16}D + \frac{1}{2}E\right)f^2 - \left(\frac{3}{32}D + \frac{3}{8}E\right)f^3$$

Table S3. Mass number analysis for the product methane in the photocatalytic tests under $^{13}CO_2$, H_2, and D_2O to produce $^{13}CH_4$, $^{13}CH_3D$, $^{13}CH_2D_2$, $^{13}CHD_3$, and $^{13}CD_4$ with the molar amount of *a*, *b*, *c* , *d*, and *e*, respectively.[*1,*2]

m/z	15	16	17	18	19	20	21
$^{12}CH_4$	$\frac{1}{100}fa$	$\frac{1}{100}a$					
$^{13}CH_4$	$\frac{1}{400}fb$	$fa + \frac{3}{400}fb$	$a + \frac{1}{100}b$				
$^{13}CH_3D$		$\frac{1}{4}fb + \frac{1}{200}fc$	$\frac{3}{4}fb + \frac{1}{200}fc$	$b + \frac{1}{100}c$			
$^{13}CH_2D_2$			$\frac{1}{2}fc + \frac{3}{400}fd$	$\frac{1}{2}fc + \frac{1}{400}fd$	$c + \frac{1}{100}d$		
$^{13}CHD_3$				$\frac{3}{4}fd + \frac{1}{100}fe$	$\frac{1}{4}fd$	$d + \frac{1}{100}e$	
$^{13}CD_4$					*fe*		*e*
Σ			= *A*	= *B*	= *C*	= *D*	= *E*

[*1] The *f* value is the fragment ratio for natural methane, i.e. intensity ratio of peak at *m/z* = 15 to that at *m/z* = 16. The *f* value was assumed to be equal for $^{13}CH_4$. The observed *f* value for $^{13}CH_4$: 0.691.

[*2] *A*, *B*, *C*, *D*, and *E* values are the intensity in mass chromatogram at *m/z* = 17, 18, 19, 20, and 21, respectively.

References

[1] H. Zhang, T. Itoi, T. Konishi, Y. Izumi, Dual Photocatalytic Roles of Light: Charge Separation at the Band Gap and Heat via Localized Surface Plasmon Resonance To Convert CO_2 into CO over Silver–Zirconium Oxide. *J. Am. Chem. Soc.* **2019**, *141*(15), 6292–6301.

[2] H. Zhang, T. Itoi, K. Niki, T. Konishi, Y. Izumi, Dual Origins of Photocatalysis: Light-Induced Band-Gap Excitation of Zirconium Oxide and Ambient Heat Activation of Gold to Enable $^{13}CO_2$ Photoreduction/Conversion. *Catal. Today* **2020**, 356, 544–556.

[3] H. Zhang, Y. Izumi, Why Is Water More Reactive Than Hydrogen in Photocatalytic CO_2 Conversion at Higher Pressures? Elucidation by Means of X-Ray Absorption Fine Structure and Gas Chromatography-Mass Spectrometry. *Front. Chem.* **2018**, *6*, 408-1–408-7.

[4] Y. Yoshida, T. Itoi, Y. Izumi, Preferential Photooxidation of CO in Hydrogen across the Crystalline Face Boundary over Spheroidal ZnO Promoted by Cu Ions. *J. Phys. Chem. C* **2015**, *119*(37), 21585–21598.

[5] M. Morikawa, N. Ahmed, Y. Yoshida, Y. Izumi, Photoconversion of Carbon Dioxide in Zinc–Copper–Gallium Layered Double Hydroxides: The Kinetics to Hydrogen Carbonate and Further to CO/Methanol. *Appl. Catal. B* **2014**, *144*, 561–569.

[6] J. A. Bearden, X-Ray Wavelengths. *Rev. Modern Phys.* **1967**, *39*(1), 78–124.

[7] H. Zhang, S. Kawamura, M. Tamba, T. Kojima, M. Yoshiba, Y. Izumi, Is Water More Reactive Than H_2 in Photocatalytic CO_2 Conversion into Fuels Using Semiconductor Catalysts Under High Reaction Pressure? *J. Catal.* **2017**, *352*, 452–465.

[8] M. Vaarkamp, H. Linders, D. Koningsberger, *XDAP Version 2.2.7*, XAFS Services International, Woudenberg, The Netherlands, 2006.

[9] *CRC Handbook of Chemistry and Physics*, 96th ed. (W. M. Haynes, Ed.), CRC Press: Boca Raton, 2015; p 4-124, 4-150, 12-216.

[10] E. Groppo, C. Prestipino, C. Lamberti, R. Carbpmo, F. Boscherini, P. Luches, S. Valeri, S. D'Addato, O K-edge X-Ray Absorption Study of Ultrathin NiO Epilayers Deposited In Situ on Ag(0 0 1). *Phys. Rev. B* **2004**, *70*, 165408-1–165408-6.

[11] E. Sevillano, H. Meuth, J. J. Rehr, Extended X-Ray Absorption Fine Structure Debye–Waller Factors. I. Monoatomic Crystals. *Phys. Rev. B* **1979**, *20*, 4908–4911.

[12] G. Beni, P. M. Platzman, Temperature and Polarization Dependence of Extended X-Ray Absorption Fine-Structure Spectra. *Phys. Rev. B* **1976**, *14*, 1514–1518.

[13] C. Clavero, Plasmon-Induced Hot-Electron Generation at Nanoparticle/Metal-Oxide Interfaces for Photovoltaic and Photocatalytic Devices. *Nat. Photonics* **2014**, *8*, 95–103.